PHYSICAL REVIEW B **91**, 245129 (2015)

Fermi surface instabilities in $CeRh_2Si_2$ at high magnetic field and pressure

A. Palacio Morales,[1,2] A. Pourret,[1,2,*] G. Seyfarth,[3,4] M.-T. Suzuki,[5] D. Braithwaite,[1,2] G. Knebel,[1,2] D. Aoki,[1,2,6] and J. Flouquet[1,2]

[1]*Univ. Grenoble Alpes, INAC-SPSMS, F-38000 Grenoble, France*

[2]*CEA, INAC-SPSMS, F-38000 Grenoble, France*

[3]*Univ. Grenoble Alpes, LNCMI, F-38042 Grenoble Cedex 9, France*

[4]*CNRS, Laboratoire National des Champs Magnétiques Intenses LNCMI (UJF, UPS, INSA), UPR 3228, F-38042 Grenoble Cedex 9, France*

[5]*RIKEN Center for Emergent Matter Science, Hirosawa 2-1, Wako, Saitama 351-0198, Japan*

[6]*Institute for Materials Research, Tohoku University, Oarai, Ibaraki 311-1313, Japan*

(Received 12 March 2015; revised manuscript received 12 May 2015; published 15 June 2015)

We present thermoelectric power (TEP) studies under pressure and high magnetic field in the antiferromagnet $CeRh_2Si_2$ at low temperature. Under a magnetic field, large quantum oscillations are observed in the TEP, $S(H)$, in the antiferromagnetic phase. They suddenly disappear when entering in the polarized paramagnetic state at H_c, pointing out an important reconstruction of the Fermi surface. Under pressure, S/T increases strongly at low temperature near the critical pressure P_c, where the antiferromagnetic (AF) order is suppressed, implying the interplay of a Fermi surface change and low-energy excitations driven by spin and valence fluctuations. The difference between the TEP signal in the polarized paramagnetic state above H_c at ambient pressure and in the pressure-induced paramagnetic state above P_c can be explained by different Fermi surfaces. Band-structure calculations at $P = 0$ stress that in the AF phase the $4f$ contribution at the Fermi level (E_F) is weak, while it is the main contribution in the paramagnetic domain. In the polarized paramagnetic phase the $4f$ contribution at E_F drops. Large quantum oscillations are observed in the antiferromagnetic state while these disappear in the polarized state above H_c. Comparison is made to the $CeRu_2Si_2$ series highly studied for its (H,T) phase diagram.

DOI: 10.1103/PhysRevB.91.245129 PACS number(s): 71.18.+y, 71.27.+a, 72.15.Jf, 75.30.Kz

I. INTRODUCTION

The interplay among spin fluctuations, valence fluctuations, and charge ordering with Fermi surface (FS) instabilities is a key point for the understanding of quantum criticality in itinerant electronic systems. Heavy fermion materials are important examples as their low renormalized characteristic temperature gives the opportunity to switch, for example, from long-range antiferromagnetic (AF) to paramagnetic (PM) ground states under moderate pressure (P) of a few GPa and to recover, by applying magnetic field (H), a polarized paramagnetic state (PPM) above the AF-PM transition at H_c [1]. An additional particularity is that the magnetically polarized phase at $H > H_c$ is often associated with the possibility of a FS reconstruction. This is characteristic of a PPM phase with a FS quite different from the PM ones. Up to now, the $CeRu_2Si_2$ series is the fingerprint example of these phenomena [2,3]. Here we present the effects of H and P on the thermoelectric power (TEP) of $CeRh_2Si_2$. The aim is to study a system where the magnetic structure of the AF phase has been fully determined [4], the (H,T) phase diagram is established [5–7], and a FS instability under pressure is well established by previous de Haas van Alphen (dHvA) experiments [8–11].

Figure 1 represents the main features of the $CeRh_2Si_2$ (H, T, P) phase diagram as measured from our TEP. On cooling at $H = 0$ and $P = 0$, $CeRh_2Si_2$ shows a first AF1 transition at $T_{N1} = 36$ K characterized by the wave vector $q_1 = (\frac{1}{2},\frac{1}{2},0)$. The magnetic structure is changing at $T_{N2} = 25$ K and in the second AF2 phase, an additional wave vector $q_2 = (\frac{1}{2},\frac{1}{2},\frac{1}{2})$ appears [4]. The sublattice magnetization (M_0) per Ce atom is near $1.5\mu_B$ and the Sommerfeld coefficient $\gamma = \frac{C}{T}$ extrapolated at $T \to 0$ K is only 23 mJ K^{-2} mol^{-1}. However, if the system would not order magnetically, the entropy balance at T_{N1} suggests an extrapolation of γ for the PM phase near 400 mJ K^{-2} mol^{-1} [12,13]. $CeRh_2Si_2$ belongs to the heavy fermion compounds with the occurrence of strong magnetic correlations by developing a large molecular field $H_{\rm int}$ [7] which is at the origin of the drop of the γ term of the specific heat. Another interesting feature is that the dominant Ising character with M_0 aligned along the c axis governs the magnetic structure properties while the Pauli susceptibility in low field is almost isotropic as if there is a decoupling between Ising local moments and the behavior of the itinerant electrons [5].

The AF2 phase disappears under pressure at $P_c' \sim 5$ kbar while the AF1 phase is suppressed at $P_c \sim 10$ kbar [4,8,12,14,15]. Under magnetic field the AFM is suppressed (for $T < 18$ K) by a cascade of first-order transitions AF2 $\to$ AF3 $\to$ PPM with two critical metamagnetic fields $H_{2-3} = 25.7$ T and $H_c = 26$ T [5,6]. As the AF3 phase exists in a narrow magnetic field domain, the main focus will be put later on the change between the AF and the PPM phases. Various macroscopic measurements show that at high magnetic field above H_c, the PPM ground state differs from the PM one [7]. Up to now, at ambient pressure, FS studies have been restricted to the AF phase, i.e., to $H < H_c$ [8]. Under pressure, FS measurements have been mainly performed with $H \perp c$ axis in the basal plane along [100], and FS changes have been observed at P_c' and P_c [8–10,15]. A rough interpretation suggests a localized description of the $4f$ electrons below P_c and an itinerant description above P_c [8].

*alexandre.pourret@cea.fr

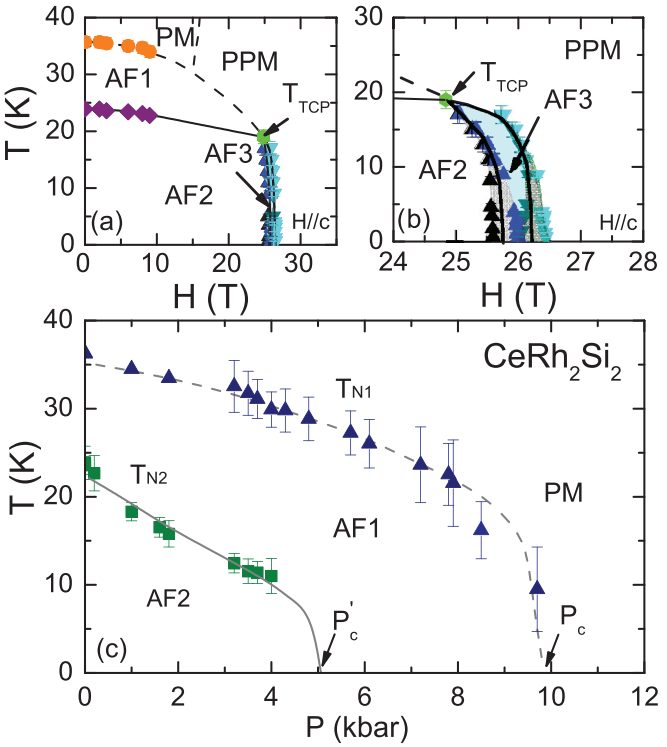

FIG. 1. (Color online) (a) (T,H) phase diagram of $CeRh_2Si_2$ drawn from field and temperature dependence of TEP for $H \parallel c$. (b) Magnification of the (T,H) phase diagram near the suppression of the magnetic order. The light gray and the gray areas indicate the field-hysteresis evolution of the transition from AF2 to AF3 and from AF3 to PPM. The blue areas in these phase diagrams show the narrow AF3 phase. (c) (T,P) phase diagram of $CeRh_2Si_2$ drawn from temperature-dependent TEP measurements, $S(T)$, with $J \parallel a$ at different pressures. The triangles show the PM-AF1 transition and the squares show the AF1-AF2 one. The error bars correspond to the width of the transition. The suppression of the AF2 and AF1 phases was estimated at $P_c' \sim 5$ kbar and $P_c \sim 9.8$ kbar, respectively. The dashed and solid lines represent second- and first-order phase transitions, respectively.

II. EXPERIMENTAL DETAILS

High-quality single crystals of $CeRh_2Si_2$ were grown using the Czochkralski method in a tetra-arc furnace. Single-crystal ingots were oriented by Laue photograph and were cut by a spark cutter. No heat treatment was done for the present samples. The sample quality was checked by resistivity measurements. The residual resistivity ratio (RRR) is in the range from 30 to 100. The highest quality sample was used for quantum oscillation measurements.

The TEP study was performed with $H \parallel c$ in order to reach the PPM regime at $P = 0$. The experiment was performed in longitudinal (thermal gradient $\nabla T \parallel c$ axis) and transverse configurations ($\nabla T \parallel a$ axis). H scans were done with a conventional superconducting magnet ($H < 16$ T) and with a resistive magnet at the Laboratoire National des Champs Magnétiques Intenses laboratory ($H < 28$ T). Zero-magnetic-field measurements under pressure were performed in a piston cylinder cell. Details of the experimental realization of the high-pressure experiment can be found in Ref. [16].

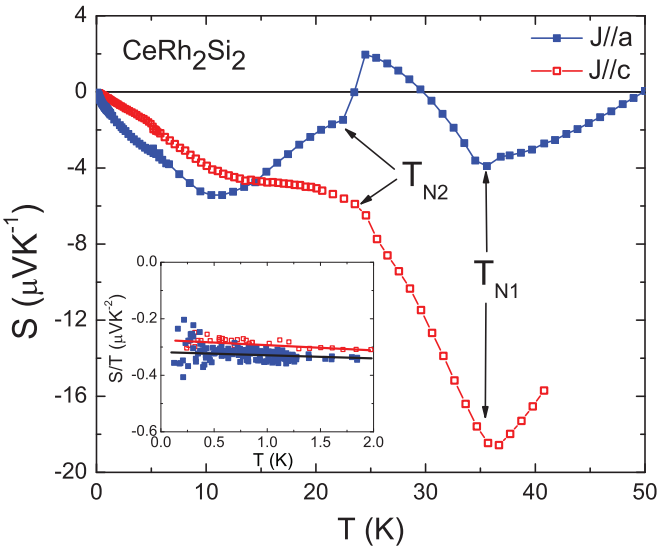

FIG. 2. (Color online) Temperature dependence of the TEP $S(T)$ for $J \parallel a$ (solid symbols) and $J \parallel c$ (open symbols). The inset shows that $S(T)/T$ is constant below 2 K for both configurations. The straight red and black lines of the inset indicate the extrapolation of $S(T)/T$ for $T \to 0$ in the $J \parallel c$ and $J \parallel a$ configurations, respectively.

III. RESULTS

A. Temperature and pressure dependence

Figure 2 shows the temperature dependence of TEP at ambient pressure for both $J \parallel a$ and $J \parallel c$ configurations at $H = 0$. In both cases the TEP shows abrupt changes in the T dependence at the magnetic transitions. At very low temperature below a minimum at $T^* \sim 10$ K, the TEP is mainly isotropic while a strong anisotropy is detected above T^*. The inset of Fig. 2 shows the temperature variation of S/T below $T = 2$ K. The quasiconstant $S(T)/T$ below 2 K is the signature of a Fermi liquid behavior in the AF state of $CeRh_2Si_2$. The extrapolation of the measurement to $T = 0$ gives $S(T)/T \sim -0.3\ \mu\text{V K}^{-2}$ for both configurations corresponding to an isotropic heat transport. This rather small value of S/T for a heavy fermion compound associated with $\gamma = 23$ mJ mol^{-1} K^{-2} of the specific heat gives $q = \frac{S}{T}\frac{N_{Av}e}{\gamma} = 1.2$, where N_{Av} is the Avogadro number and e is the electronic charge [17]. This ratio is inversely proportional to the number of carriers per unit formula, $n = 1/q = 0.8$, which is close to unity expected for normal heavy fermion metals.

Furthermore, the usual positive value of S/T in the limit $T \to 0$ K observed for many Ce-based heavy fermion compounds is not recovered. Clearly, the creation of new small Brillouin zones and its associated FS reconstruction modify the band structure and thus the energy derivative of the density of states, which is directly linked to the TEP signal. As discussed below, the Ce-4f contribution to the density of states at the Fermi level is small in the AF phase.

Typical $S(T,P)$ curves are presented in Fig. 3(a). From the marked signature of $S(T)$ at T_{N1} and T_{N2}, the (T,P) phase diagram of $CeRh_2Si_2$ was drawn in Fig. 1, which is in good agreement with previous reports [4,9,14,15]. $S(T)$ and $S(T)/T$ at low temperature for different pressures are represented in

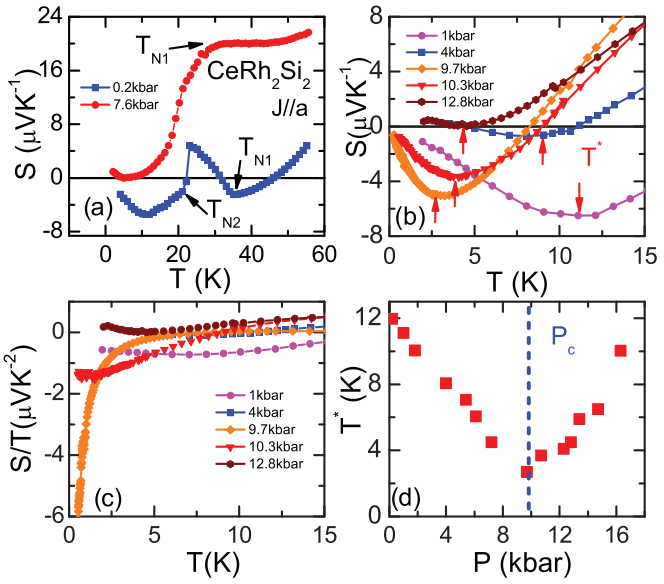

FIG. 3. (Color online) (a) Temperature dependence of the TEP, $S(T)$, for $J \parallel a$ at $P = 0.2$ kbar and $P = 7.6$ kbar for $CeRh_2Si_2$. (b) $S(T)$ for different pressures at low temperature for $J \parallel a$. The temperature positions, T^*, of the minimum of $S(T)$ are indicated by red vertical arrows. (c) $S(T)/T$ at low temperature for different pressures. The extremely large value of $S(T)/T$ for $T \to 0$ at $P = 9.7$ kbar reflects the proximity to the critical pressure P_c. (d) Pressure dependence of T^*. T^* marks the entrance in a coherent low-temperature regime which is significantly reduced precisely at the critical pressure P_c.

Figs. 3(b) and 3(c), respectively. The extremely large value of $S(T)/T$ for $T \to 0$ at $P = 9.7$ kbar reflects the proximity to the critical pressure P_c. The entrance in a coherent regime is marked by a well-defined (local) minimum at T^*, as shown in Fig. 3(b). $T^*(p)$ is minimal right at the critical pressure P_c, where the AF order is suppressed, as shown in Fig. 3(d).

The pressure dependencies of the TEP at 10 K and 3 K are plotted in Fig. 4(a). Below 0.8 kbar, rather similar values of S/T are obtained. However, in the critical regime (8–13 kbar) large differences exist between $T = 10$ K and $T = 3$ K, in agreement with the occurrence of a deep negative minimum on cooling close to P_c. In this pressure range, the characteristic electronic energy drops on approaching P_c, as clearly observed in the decrease of T^* [Fig. 3(d)] and in the shrinking of the low-temperature domain (at P_c lower than 8 K), where the AT^2 Fermi liquid resistivity is detected [15].

Furthermore, in Fig. 4, we have plotted the pressure dependence of (b) the residual resistivity ρ_0, (c) the A coefficient (taken from Ref. [9]), and (d) the dHvA frequencies (from Ref. [10]). The signatures of the TEP at P_c' and P_c correspond to clear changes in the residual resistivity and dHvA frequencies. The inelastic T^2 term of the resistivity has a marked maximum, while in Ref. [15] a plateau was reported. Further experiments are necessary to clarify the origin of the anomalies detected in the resistivity close to P_c for electrical current $J_e \parallel a$ and $J_e \parallel c$ [9].

The important observations in the TEP are that (i) S/T changes sign from a negative to a positive value at P_c', (ii) S/T has a deep negative minimum at P_c, and (iii) recovers

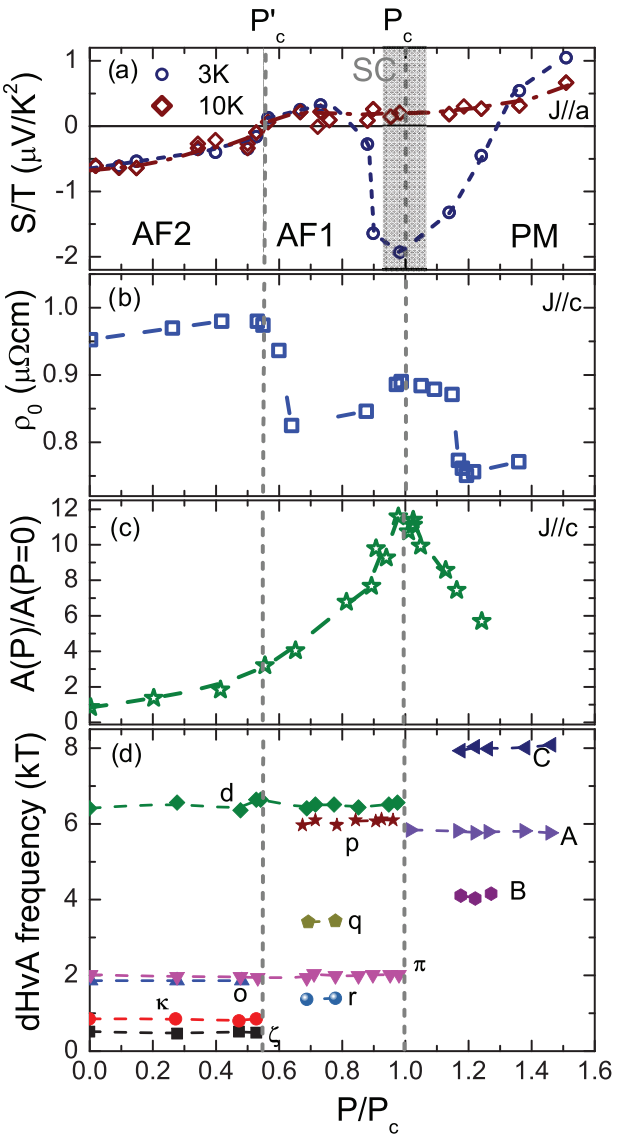

FIG. 4. (Color online) Observation of FS changes under pressure by different probes: (a) TEP over temperature, S/T, at $T = 3$ K (open blue circles) and at $T = 10$ K (red diamonds); (b) residual resistivity ρ_0 (open blue squares); (c) normalized A coefficient $A(P)/A(P = 0)$ (open green stars) [9]; and (d) dHvA frequencies obtained for $H \parallel a$ (solid symbols) [10] as a function of pressure P/P_c.

the common positive sign of the TEP for Ce heavy fermion compounds above P_c. The drastic change of S around P_c is clearly associated with the large FS reconstruction detected at P_c [Fig. 4(d)]. At least the rather large pressure width of the $S(P)$ anomaly ($\Delta p \sim 0.3$ GPa) coincides with the pressure range of the enhancement of the A coefficient. $CeRh_2Si_2$ is thus a key example of the consequence of the interplay between electronic fluctuations (as we discuss spin and valence fluctuations) at P_c and a FS instability.

B. Field dependence

Next we focus on the field dependence of TEP at $P = 0$. As in this multi-band heavy fermion system the signal of each subband is weighted by its respective electrical conductivity

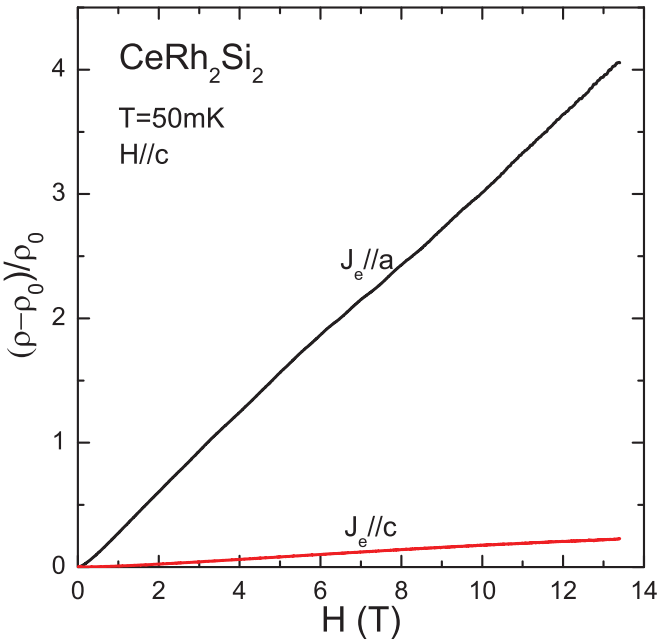

FIG. 5. (Color online) $(\rho - \rho_0)/\rho_0$ as a function of the magnetic field for transverse ($RRR = 100$) and longitudinal ($RRR = 30$) configurations. A strong magnetoresistance increase is observed in the high-quality sample.

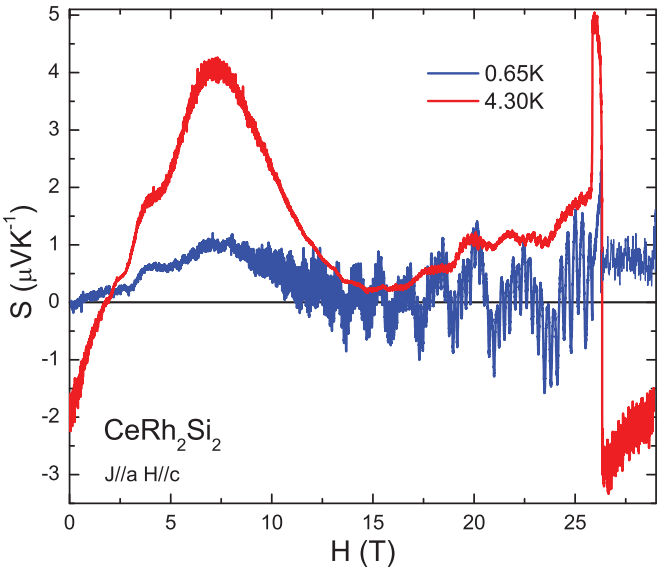

FIG. 6. (Color online) Isothermal TEP measurements as a function of magnetic field $S(H)|_T$ at different temperatures for the transverse configuration. The low-temperature curve shows the suppression of quantum oscillations at the PPM phase. The higher harmonic content of the Seebeck oscillations imparts a characteristic sawtooth shape to the oscillations.

[18], a large magnetoresistivity may reveal different signatures. In our case, for the transverse configuration, an excellent crystal was used with $RRR \sim 100$ while for the longitudinal configuration a crystal with only $RRR \sim 30$ was measured. Figure 5 emphasizes the large magnetoresistivity detected for $J_e \parallel a$ by comparison to the longitudinal one, $J_e \parallel c$. While for the transverse magnetoresistance $(\rho - \rho_0)/\rho_0 \approx 4$, we find for the longitudinal magnetoresistance only ≈ 0.2 for a field of 13 T. It is also surprising that the transverse magnetoresistance does not show a H^2 field dependence, as expected for the high-field limit in a single-band picture, but is linear for $H >$ 9 T, where small Shubnikov de Haas oscillations appear. This linear magnetoresistance already indicates that a single-band picture does not describe the transport properties correctly. The strong magnetoresistance indicates the possible entrance in the high-field region with $\omega_c\tau \gg 1$, ω_c being the cyclotron frequency and τ the scattering time, respectively. Contrary to the transverse magnetoresistance, the longitudinal one is rather small. It changes curvature from convex to concave around 7 T and for high field a saturation of the magnetoresistance is expected, in agreement with the small intrinsic longitudinal magnetoresistance. In addition to the "classical" difference in the magnetoresistance there is for both configurations an additional inelastic response, notably due to spin fluctuations.

The consequence of this anisotropic magnetoresistance on TEP is that, for the transverse configuration, features associated with the entrance in the collisionless regime with dominating orbital contribution were observed already for $T \sim 6$ K, as shown by the large quantum oscillations in the TEP for the transverse configuration up to 4.3 K (see Fig. 6). Surprisingly, already at $T = 4.3$ K for $H \sim 5$ T quantum oscillations are detected up to $H_c \sim 26$ T, while no quantum oscillation signal is detected above H_c. To get information of the FS properties of $CeRh_2Si_2$, we performed a fast Fourier transform (FFT) of the Seebeck signal. The spectrum for the AF2 phase of $CeRh_2Si_2$ for the highest quality sample (transverse configuration) is represented in Fig. 7. No oscillations have been observed in the spectrum for the

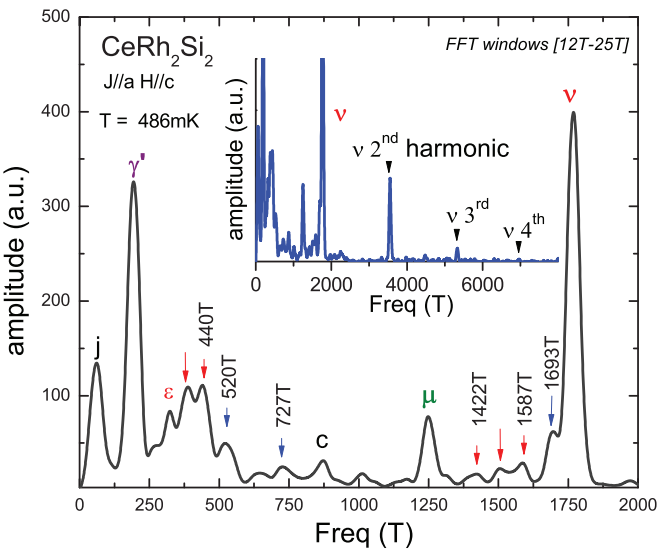

FIG. 7. (Color online) FFT spectrum of the TEP signal of $CeRh_2Si_2$ at the lowest temperature $T = 486$ mK for a field range from 12 to 25 T, i.e., in the AF2 state. The known frequencies are named following Ref. [8], the new ones are indicated by blue arrows, and the frequencies due to magnetic breakdown are shown by red arrows. The inset shows the main frequency ν and its harmonics up to the fourth one.

TABLE I. List of quantum oscillation frequencies in the $AF2$ phase for $H \parallel c$ obtained from dHvA measurements of Ref. [8] and from $S(H)$ at $T = 486$ mK for the transverse configuration.

Frequencies of the $AF2$ phase (T)		
Branches	dHvA (Ref. [8]), 13–16.9 T	$S(H)$, 12–25 T
l	44	
k	56	
j	66	61
	77	
α''	81	
γ'	137	
γ	184	194
ε	327	324
		387
		440
		520
		727
c	804	870
μ	1160	1249
		1422
		1505
		1587
		1693
ν	1770	1768
a	7560	

AF3 and the PPM phase above H_c. The higher harmonic content of the TEP oscillations (up to the fourth harmonics of ν has been observed) imparts a characteristic sawtooth shape to the oscillations. The frequencies in the TEP signal and those reported previously from dHvA experiments [8] for $H \parallel c$ are listed in Table I. The frequencies detected in TEP are in good agreement with those from dHvA, although TEP measurements cannot detect the low frequencies of the FS of the AF2 state. Similarly, the various masses extracted from the TEP branches [16] are similar to the ones obtained in the dHvA experiments [8]: The measured effective masses range from $0.64\,m_0$ for the γ branch to $5m_0$ for the μ branch [8,11]. However, in TEP additional frequencies have been detected corresponding to orbits of the AF2 FS which have been never detected except for frequencies close to 387 and 1505 T, which probably correspond to a magnetic breakdown [16]. Careful analysis of the FS determination in relation with new band-structure calculation will be presented separately. Experimental studies of the TEP quantum oscillations can be found in Ref. [16].

As shown in Fig. 8, the transitions AF2-AF3 and AF3-PPM are characterized by a rapid change in the absolute value of the TEP coefficient and by a hysteretic behavior confirming the first-order nature of the transitions. At the lowest temperature ($T = 0.65$ K), $S(H)$ shows large quantum oscillations up to the AF2-AF3 transition at $H_{2-3} = 25.7$ T. At the AF3-PPM transition at $H_c = 26$ T a very sharp drop of $S(H)$ appears. At higher temperature ($T = 13.6$ K), $S(T)$ decreases sharply at H_{2-3} and H_c. For $T > T_{TCP} = 17$ K, the transition AF1-PPM becomes broad with no hysteresis and the broadening marks the suppression of the AF order with a second-order phase

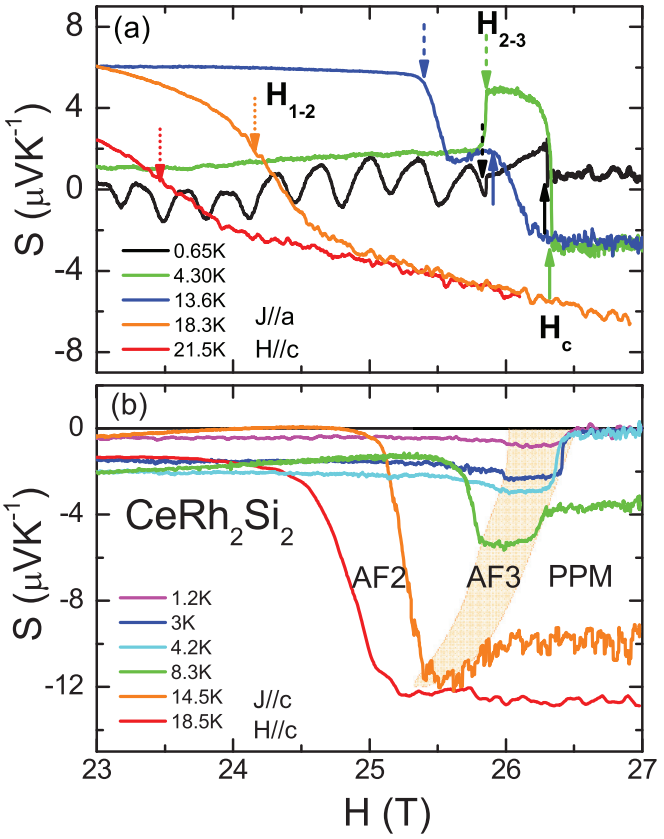

FIG. 8. (Color online) Isothermal TEP, $S(H)$, at different temperatures focusing on the high-field range. (a) For $J \parallel a$, the metamagnetic transitions H_{2-3} and H_c are characterized by a two-step anomaly and symbolized for each temperature by dashed and solid vertical arrows, respectively. The AF1-PPM transition (H_{1-2}) which takes place for $T > T_{TCP} = 17$ K is marked by a dotted vertical arrow. (b) For $J \parallel c$, the evolution of the AF3, delimited by the orange area, is represented.

transition. For the longitudinal configuration [see Fig. 8(b)], the evolution of the AF3 phase can also be observed. The collapse of the AF3 phase occurs at $T \sim T_{TCP}$. The (H, T) phase diagrams determined with these different anomalies (with $\nabla T \parallel$ c and $\nabla T \parallel a$) are in excellent agreement, as can be seen in Fig. 1 [5–7]. The slight difference in the position of the AF2 boundary is only due to the difficulty in selecting precisely the $S(T)$ anomalies above T_{TCP}.

IV. DISCUSSION

A. Pressure and magnetic field dependence

Drastic changes of the TEP are observed on crossing H_c and P_c. Figure 9 shows at $T = 3$ K the respective P and H dependence of S as a function of the reduced parameters $\frac{P}{P_c}$ and $\frac{H}{H_c}$. The large width of the P anomaly across P_c contrasts with the sharp feature of the field scan at H_c. In magnetic field scans, two main features occur: (i) the disappearance of the quantum oscillations above H_c, pointing out a major Fermi surface change connected with the unfolding of the Brillouin zone; (ii) a step in the macroscopic signal reflecting clearly the strong metamagnetic transition at H_c (magnetization jump

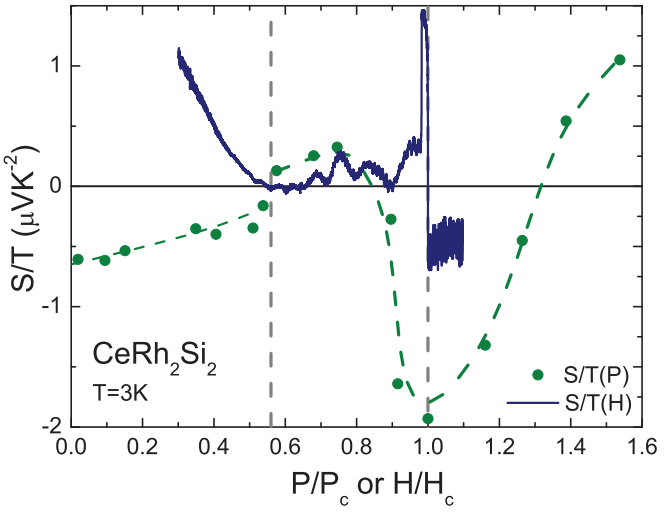

FIG. 9. (Color online) S/T for the transverse configuration as a function of magnetic field H/H_c and as a function of pressure P/P_c in a blue continuous line and green dots, respectively.

$\Delta M \sim 1.2\mu_B$ per Ce atom) coupled with a strong change of dominant heat carriers. Under pressure, the quantum phase transition at P_c is marked by a broad negative signature directly linked with anomalies in the residual resistivity, in the Hall effect [15], and in the P dependence of the sublattice magnetization M_0, which drastically collapses [4]. Thermal expansion measurements give evidence that the quantum phase transition at P_c is weakly first order [19]. Also, the T domain of the AT^2 dependence of the resistivity does not shrink to zero, as predicted and observed for the AF second-order quantum critical point [1]: A T^2 dependence of ρ is observed for all pressures [9,15].

B. Fermi surface and electronic structure

The first-order nature of the transition at P_c appears in good agreement with the drastic change of the FS reported in dHvA experiments [8–10]. Far below P_c, at ambient pressure, the $4f$ electrons are considered to be localized as no main $4f$ contribution appears at the Fermi level. The angular dependence of the large dHvA frequencies can be *de facto* explained by those of $LaRh_2Si_2$. Due to the magnetic order, the magnetic Brillouin zone is 8 times smaller than that of the body-centered tetragonal Brillouin zone. The density of states, calculated by a LDA + U method with the $U = 5$ eV in the framework of the full potential linearized augmented plane wave (FLAPW) method, is represented in Fig. 10. We performed the calculations self-consistently determining the charge density and the density matrices for the nonmagnetic state and assuming Ce-f^1 occupation for the $|j = 5/2, j_z = 5/2\rangle$ orbital of the density matrices for the magnetic state, taking the eight $CeRh_2Si_2$ formula magnetic unit cells for the $4q$-magnetic order with the proper magnetic alignment [4]. For the $4q$-AF state, there is no direct contribution from the Ce-$4f$ states at the FS. However, if the PM state will be the ground state at $P = 0$, the $4f$ states will be located around the Fermi level and have large contribution to the FS. This new approach opens the possibility to understand the FS topology with an

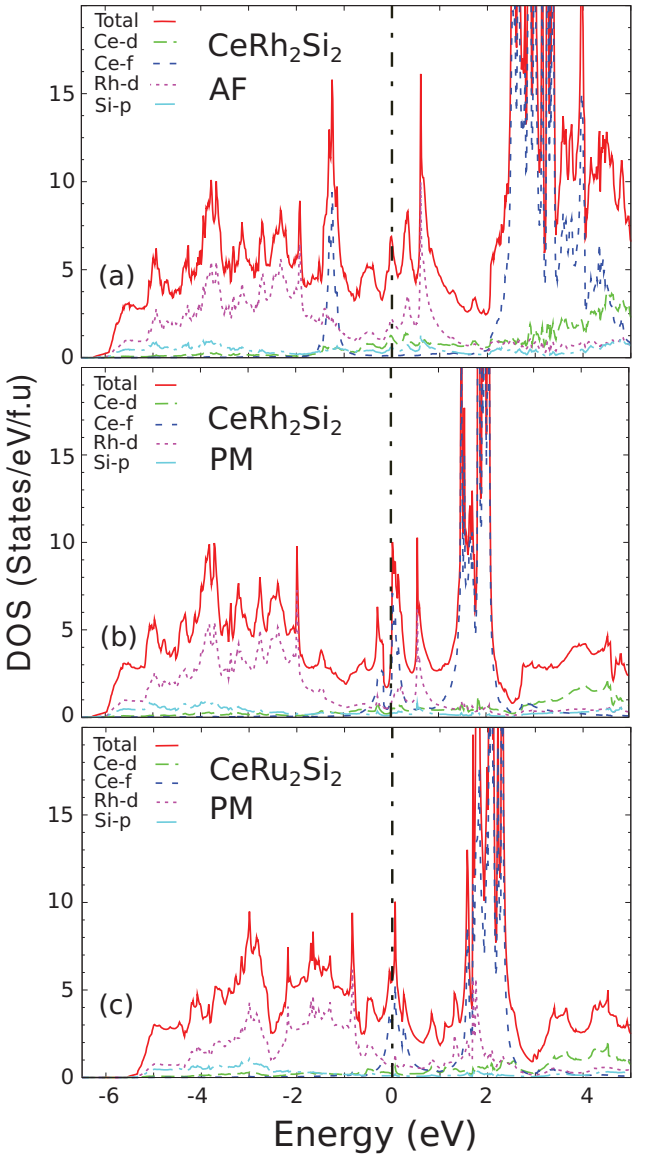

FIG. 10. (Color online) Comparison between the densities of states determined by LDA + U calculation in $CeRh_2Si_2$ and $CeRu_2Si_2$: Panels (a) and (b) correspond to the $4q$-AF and PM phases of $CeRh_2Si_2$, respectively, and (c) corresponds to the PM state of $CeRu_2Si_2$. In the $4q$-AF state of $CeRh_2Si_2$, no Ce-$4f$ contribution appears at the FS; contrarily, for the PM state, f states are now located around the Fermi level and have a large contribution to the FS. The densities of states in the PM state of $CeRu_2Si_2$ and $CeRh_2Si_2$ are very similar.

initial itinerant picture by incorporating the large molecular field ($H_{\rm int}$) created by the robust AF (concomitant large T_N and M_0) and the creation of a new Brillouin zone. Let us point out that this PM density of states of $CeRh_2Si_2$ at $P = 0$ is quite similar to the one obtained for $CeRu_2Si_2$. The extension of the calculation for $CeRu_2Si_2$ to strong magnetic polarization shows that in $CeRu_2Si_2$ a deep shift of the $4f$ level from the FS occurs above its metamagnetic transition [20].

It is appealing to propose that the sign change of S/T at 3 K right at P_c' marks the switch from a localized to an itinerant nature of the $4f$ electrons. This behavior has been proposed for

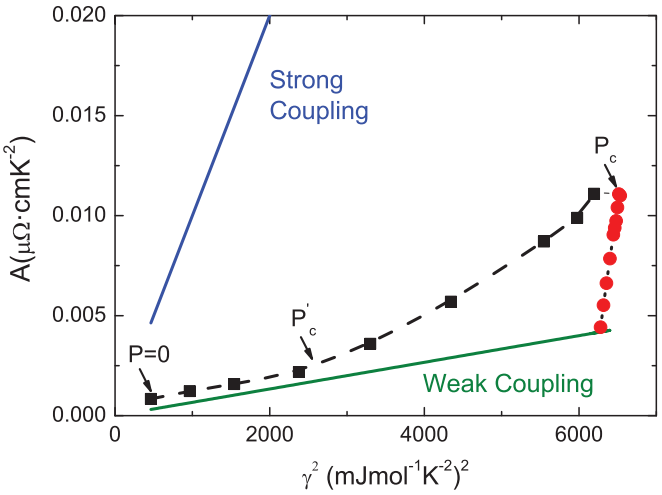

FIG. 11. (Color online) A coefficient (values obtained from Ref. [15]) as a function of the square of the electronic specific heat γ^2 (from Ref. [12]). The blue and green lines represent the limits for strong-coupling and weak-coupling behaviors, respectively. The black square symbols correspond to the AF phase and the red circles to the PM phase.

a Kondo lattice inside the AF domain with the particularity of very low-energy strong local fluctuations driven by a Lifshitz transition [21]. Experimental evidence for such a scenario has been reported for the system $CeRu_2(Si_xGe_{1-x})_2$ [3]. However, as shown in Fig. 4(d), no drastic change of dHvA frequencies has been observed and the d and π branches are almost not affected at P_c'. The κ branch has not been observed above P_c'. These small differences in the observed branches below and above P_c' seem to reflect the Brillouin zone change between the AF1 and AF2 phases due to the different ordering vectors. Furthermore, there is no signature of an energy decrease of the excitations in TEP. As the transition AF2-AF1 is of first order at P_c' [7,8], the possibility of an additional electronic Lifshitz transition at P_c' remains. There is a strong deviation from AT^2 resistivity behavior at P_c' but it can be explained in the frame of AF2-AF1 inhomogeneous mixing [15]. There is no doubt that above P_c the new FS is in agreement with $4f$ itinerant quasiparticles entering in the mixed valence regime just above the critical pressure P_c.

C. Entering a mixed valent state above P_c

At P_c, $CeRh_2Si_2$ is very close to entering the mixed valence regime, i.e., P_c close to P_v, the characteristic valence pressure [2,22]. Proofs of this proximity are given (i) by the P decrease of the magnetic anisotropy (the maximum of the susceptibility ratio between c and a axis varying from 6 at $P = 0$ to already 2 at 0.098 GPa) [23], (ii) by the strong P variation of the thermal expansion ratio $\frac{\alpha_a}{\alpha_c}$ (going from 0.23, 0.73, and 1 for $P = 0.41$, 0.77, and 1.04 kbar) [19], (iii) by the weak value of the $\frac{A}{\gamma^2}$ Kadowaki Woods (KW) ratio on both sides of P_c. The KW ratio is drawn in Fig. 11, taking the A value from Ref. [9] and γ from Ref. [12], respectively. In the case of strong coupling (Ce level degeneracy $N = 2$), $\frac{A}{\gamma^2}$ is predicted to reach 10^{-5} $\mu\Omega$ cm $(\mathrm{K\,mol/mJ})^2$, while in the case of weak coupling ($N = 6$ full Ce degeneracy) the ratio is reduced by an order of magnitude $[\frac{A}{\gamma^2} \sim \frac{10^{-5}}{N(N-1)}]\mu\Omega\mathrm{cm}(\mathrm{K\,mol/mJ})^2$ [24,25]. Due to the large strength of H_{int} for $P \ll P_c$ and the low contribution of the $4f$ localized component at the Fermi level, $\frac{A}{\gamma^2}$ is near the weak coupling limit. Strong increase of KW ratio is observed on approaching P_c, but on increasing slightly the pressure above P_c $\frac{A}{\gamma^2}$ tends again towards the weak coupling case. The interplay of rather comparable Kondo and AF correlations at $P = 0$ restores a local Ce picture far below P_c with well-resolved crystal-field levels [26]. However, on increasing pressure, assuming a P invariance of the bare crystal field (with characteristic energy $k_B T_{CF}$), the concomitant P increase of the Kondo energy and P collapse of AF interactions leads to a quenching of the full angular momentum via the Kondo coupling. Thus, the crystal field is no more efficient to operate. A key point is that in $CeRh_2Si_2$ the magnetic anisotropy changes at P_c and the Ising character starts to collapse.

D. Comparison of the TEP of $CeRh_2Si_2$ with $CeRu_2Si_2$

It is worthwhile to compare the TEP signal of $CeRh_2Si_2$ with the one of $CeRu_2Si_2$ as this system, already in the PM state at $P = 0$ ($P_c \sim -4$ kbar), is a reference in the study of pseudometamagnetic phenomena. Pseudomagnetism in $CeRh_2Si_2$ appears above P_c for a magnetic field H_m ($H_m = 40$ T close to P_c [27]). H_m can be interpreted as a crossover continuation of the metamagnetic field H_c [2,28,29]. Expanding the volume via La or Ge doping in $CeRu_2Si_2$ leads to recovering AF long-range-order and first-order metamagnetism under magnetic field [2,3].

We focus here on the difference in magnetic response of the undoped pure lattice. At ambient pressure at the metamagnetic field $H_c \sim 26$ T, the Sommerfeld coefficient of $CeRh_2Si_2$ reaches 80 mJ K^{-2} mol^{-1}, while in $CeRu_2Si_2$ at H_m,γ reaches a value of 600 mJ K^{-2} mol^{-1}. We notice that the factor 10 between the γ values is related to the ratio of their relevant energies; then we can compare their TEP response taking into account this factor 10 in temperature analysis.

Figure 12 shows the longitudinal and transverse TEP responses of $CeRu_2Si_2$ at 260 mK by comparison to the $CeRh_2Si_2$ ones at 3 K. At H_m in $CeRu_2Si_2$ a drastic change of the FS has been reported [3,30–32] and is associated with a strong increase of A and γ right at H_m, preserving a quasiconstant $\frac{A}{\gamma^2}$ ratio. Due to the large magnetoresistivity anisotropy, the transverse and longitudinal signals have opposite sign response at H_m. However, the metamagnetic transitions present quite similar widths, $\Delta H \sim 2$ T, for transverse and longitudinal configurations. This width is quite larger than the width detected for $CeRh_2Si_2$ at H_c ($\frac{\Delta H}{H_c} \sim 0.02$). Thus, the TEP signal in $CeRh_2Si_2$ at H_c is clearly governed by the strong first-order nature of the metamagnetic transition, while the FS crossover detected at H_m in $CeRu_2Si_2$ is characteristic of a sole Lifshitz transition.

E. (H,T,P) phase diagram and conclusion

Figure 13 shows the suggested (T, H, P) phase diagram for $CeRh_2Si_2$ obtained from TEP measurements. The (T, H, $P = 0$) lines as well as the (T, $H = 0$, P) ones have been determined by TEP measurements. Due to the first-order

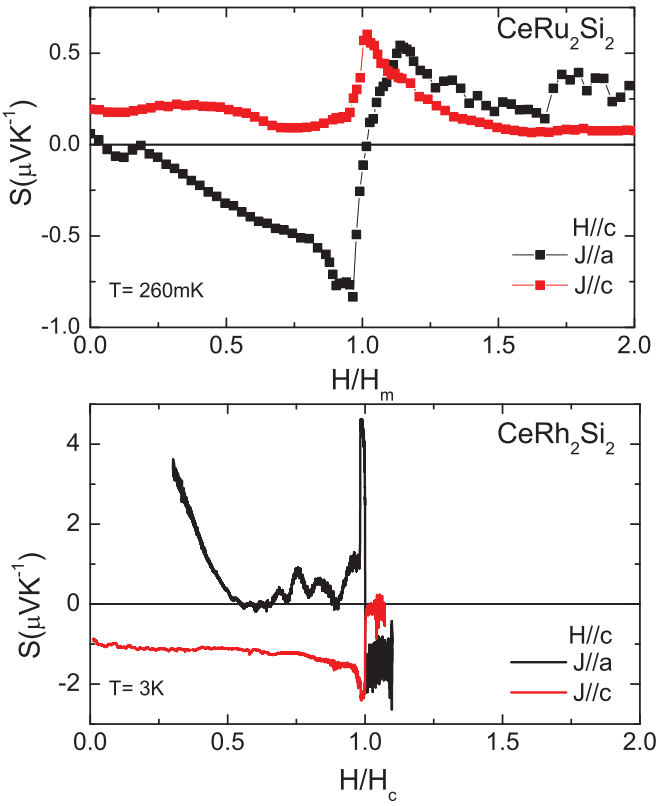

FIG. 12. (Color online) Comparison between the isothermal TEP measurements as a function of magnetic field of $CeRu_2Si_2$ and $CeRh_2Si_2$ for transverse (red symbols) and longitudinal (black symbols) configurations. The magnetic field scales of these two compounds are normalized by the critical magnetic field H_m and H_c for $CeRu_2Si_2$ and $CeRh_2Si_2$, respectively. A strong modification of the isothermal thermopower measurement has been observed at the transition in both Ce compounds.

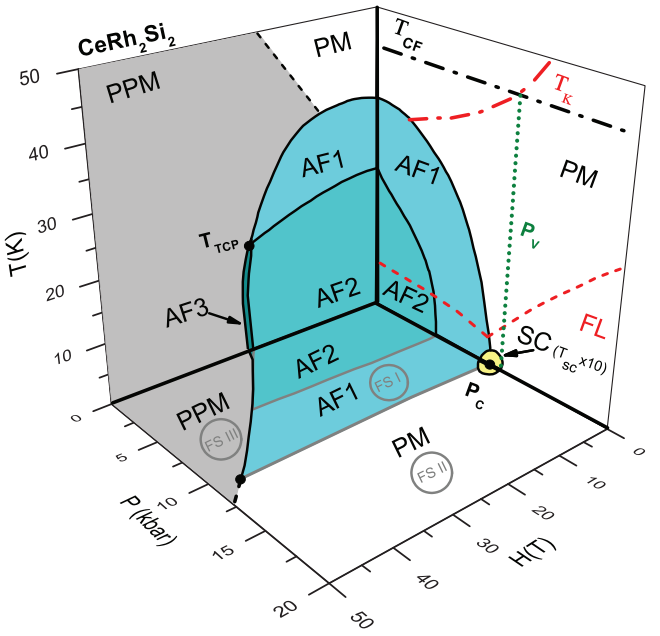

FIG. 13. (Color online) (T, H, P) phase diagram of $CeRh_2Si_2$ obtained by our TEP measurements and magnetic susceptibility measurements [7]: P_v is the characteristic valence pressure, P_c is the critical pressure, T_{CF} is the energy of the first crystal-field level, T_K is the Kondo temperature. Three different FSs (labeled FS I, FS II, and FS III) correspond to the AF, PM, and PPM states. Due to the first-order nature of the quantum phase transition at P_c, the FL regime is obeyed below the FL temperature shown by the red dashed line. In this regime, resistivity follows AT^2 law even at P_c.

nature of the quantum phase transition at P_c, the Fermi liquid (FL) temperature below which AT^2 FL law is obeyed is finite at P_c ($T^* \sim 2$ K). The lines drawn on the ($T = 0$, H, P) planes (using partly Ref. [7]) are possible guesses with H_c terminating at a critical end point with a continuation by a crossover line above P_c. Another possibility, as happens for the system $Ce(Rh_{0.92}Ru_{0.08})_2Si_2$ [33], is the collapse of H_c at P_c and thus a decoupling between H_m and H_c. In this phase diagram, the superconducting (SC) domain glued on P_c is represented; the SC territory appears to be quite narrow. Clearly, it is necessary to revisit the SC properties.

The drastic difference in the TEP between transverse and longitudinal response is connected with the difference in the magnetoresistivity. This rather strong effect under magnetic field must deserve theoretical treatment. For example, an open question is the possibility of differences in the H dependence of the hybridization.

Our main message is that AF, PM, and PPM phases have three different FSs. As with a P scan in high magnetic field ($H > H_c$ for $P \leqslant P_c$ and $H > H_m$ for $P > P_c$), no phase transition is expected; no P modification of the FS topology may occur in the PPM domain. As discussed for the pseudometamagnetism of $CeRu_2Si_2$ [20,34,35], an itinerant description on $CeRh_2Si_2$ close to P_c, whatever the strength of the magnetic field, seems to be a sound approach. To confirm the validity of our conclusions, new experiments must be realized. For example, at $P = 0$, inelastic neutron scattering measurements on single crystals will confirm whether the intersite magnetic coupling overpasses the Kondo energy and establish whether the crystal-field excitations are dispersionless. Further high-pressure experiments far above P_c will validate, or not, our proposal of the proximity of P_c and P_v. The loss of the Ising character on crossing P_c must be confirmed by microscopic measurements. By high-energy spectroscopy experiments, the pressure evolution of the $4f$ trivalent occupancy number (n_f) should be determined as well as the crystal structure. A recent advance is a precise determination of the FS at zero pressure in both PM ($T > T_N$) and AF ($T < T_N$) phases by angle-resolved photoemission spectroscopy [36]. Furthermore, a dHvA signal change at H_c on entering in the PPM phase has been recently observed directly [37].

ACKNOWLEDGMENTS

We thank H. Harima, D. Vyalikh, Y. Ōnuki, S. Araki, and P. Wölfle for many useful discussions. This work has been supported by the French ANR (Projects PRINCESS), the ERC (Starting Grant NewHeavyFermion), ICC-IMR, KAKENHI, REIMEI, and the EuromagNET II (EU Contract No. 228043). LNCMI-CNRS is member of the European Magnetic Field Laboratory (EMFL).

[1] H. Löhneysen, A. Rosch, M. Vojta, and P. Wölfle, Rev. Mod. Phys. **79**, 1015 (2007).

[2] J. Flouquet, *Progress in Low Temperature Physics* (Elsevier, Amsterdam, 2005), Vol. 15, Chap. 2, p. 139.

[3] H. Aoki, N. Kimura, and T. Terashima, J. Phys. Soc. Jpn. **83**, 072001 (2014).

[4] S. Kawarazaki, M. Sato, Y. Miyako, N. Chigusa, K. Watanabe, N. Metoki, Y. Koike, and M. Nishi, Phys. Rev. B **61**, 4167 (2000).

[5] R. Settai, A. Misawa, S. Araki, M. Kosaki, K. Sugiyama, T. Takeuchi, K. Kindo, Y. Haga, E. Yamamoto, and Y. Ōnuki, J. Phys. Soc. Jpn. **66**, 2260 (1997).

[6] H. Abe, H. Suzuki, H. Kitazawa, T. Matsumo, and G. Kido, J. Phys, Soc. Jpn. **66**, 2525 (1997).

[7] W. Knafo, D. Aoki, D. Vignolles, B. Vignolle, Y. Klein, C. Jaudet, A. Villaume, C. Proust, and J. Flouquet, Phys. Rev. B **81**, 094403 (2010).

[8] S. Araki, R. Settai, T. C. Kobayashi, H. Harima, and Y. Ōnuki, Phys. Rev. B **64**, 224417 (2001).

[9] S. Araki, M. Nakashima, and R. Settai, J. Phys. Condens. Matter **14**, L377 (2002).

[10] R. Settai, S. Araki, H. Shishido, Y. Inada, Y. Haga, E. Yamamoto, T. C. Kobayashi, N. Tateiwa, and Y. Ōnuki, J. Magn. Magn. Mater. **262**, 399 (2003).

[11] H. Abe, H. Kitazawa, and H. Aoki, J. Phys, Soc. Jpn. **67**, 1852 (1998).

[12] T. Graf, J. D. Thompson, M. F. Hundley, R. Movshovich, Z. Fisk, D. Mandrus, R. A. Fisher, and N. E. Phillips, Phys. Rev. Lett. **78**, 3769 (1997).

[13] T. Graf, M. F. Hundley, R. Modler, R. Movshovich, J. D. Thompson, D. Mandrus, R. A. Fisher, and N. E. Phillips, Phys. Rev. B **57**, 7442 (1998).

[14] R. Movshovich, T. Graf, D. Mandrus, J. D. Thompson, J. L. Smith, and Z. Fisk, Phys. Rev. B **53**, 8241 (1996).

[15] R. Boursier, Ph.D. thesis, Université Joseph Fourier, Grenoble, 2005.

[16] A. Palacio Morales, Ph.D. Thesis, Université Joseph Fourier, Grenoble, 2014.

[17] K. Behnia, D. Jaccard, and J. Flouquet, J. Phys.: Cond. Mat. **16**, 5187 (2004).

[18] R. D. Barnard, *Thermoelectricity in Metals and Alloys* (Taylor & Francis, London, 1972).

[19] A. Villaume, D. Aoki, Y. Haga, G. Knebel, R. Boursier, and J. Flouquet, J. Phys.: Condens. Matter **20**, 015203 (2008).

[20] M.-T. Suzuki and H. Harima, J. Phys. Soc. Jpn. **79**, 024705 (2010).

[21] S. Hoshino and Y. Kuramoto, Phys. Rev. Lett. **111**, 026401 (2013).

[22] S. Watanabe and K. Miyake, J. Phys. Soc. Jpn. **82**, 083704 (2013).

[23] H. Mori, N. Takeshita, N. Môri, and Y. Uwatoko, Physica B **259-261**, 58 (1999).

[24] K. Miyake, T. Matsuura, and C. Varma, Solid State Commun. **71**, 1149 (1989).

[25] N. Tsujii, H. Kontani, and K. Yoshimura, Phys. Rev. Lett. **94**, 057201 (2005).

[26] T. Willers *et al.*, Phys. Rev. B **85**, 035117 (2012).

[27] T. Hamamoto, K. Kindo, T. C. Kobayashi, Y. Uwatoko, S. Araki, R. Settai, and Y. Ōnuki, Physica B **281-282**, 64 (2000).

[28] A. Amato, D. Jaccard, J. Sierro, P. Haen, P. Lejay, and J. Flouquet, J. Low Temp. Phys. **77**, 195 (1989).

[29] A. Pourret, D. Aoki, M. Boukahil, J.-P. Brison, W. Knafo, G. Knebel, S. Raymond, M. Taupin, Y. Ōnuki, and J. Flouquet, J. Phys. Soc. Jpn. **83**, 061002 (2014).

[30] H. Aoki, M. Takashita, S. Uji, T. Terashima, K. Maezawa, R. Settai, and Y. Ōnuki, Phys. B (Amsterdam, Neth.) **206-207**, 26 (1995).

[31] S. Julian, F. Tautz, G. McMullan, and G. Lonzarich, Phys. B (Amsterdam, Neth.) **199-200**, 63 (1994).

[32] M. Boukahil, . Pourret, G. Knebel, D. Aoki, Y. Ōnuki, and J. Flouquet, Phys. Rev. B **90**, 075127 (2014).

[33] Y. Machida, K. Izawa, D. Aoki, G. Knebel, A. Pourret, and J. Flouquet, J. Phys. Soc. Jpn. **82**, 054704 (2013).

[34] K. Miyake and H. Ikeda, J. Phys. Soc. Jpn. **75**, 033704 (2006).

[35] R. Daou, C. Bergemann, and S. R. Julian, Phys. Rev. Lett. **96**, 026401 (2006).

[36] D. V. Vyalikh (unpublished).

[37] I. Sheikin (unpublished).